Published in final edited form as:
*Biochem J.* 2011 May 1; 435(3): 711–722. doi:10.1042/BJ20101726.

# Molecular interaction and functional regulation of connexin50 gap junctions by calmodulin

**Yanyi Chen**[*], **Yubin Zhou**[*], **Xianming Lin**[†], **Hing-Cheung Wong**[*], **Qin Xu**[†], **Jie Jiang**[*], **Siming Wang**[*], **Monica M. Lurtz**[‡], **Charles F. Louis**[‡], **Richard D. Veenstra**[†], and **Jenny J. Yang**[*,1]

[*]Department of Chemistry, Georgia State University, Atlanta, GA 30303, U.S.A

[†]Department of Pharmacology, SUNY Upstate Medical University, Syracuse, NY 12210, U.S.A

[‡]Department of Cell Biology and Neuroscience, University of California, 900 University Avenue, Riverside, CA 92521, U.S.A

## Abstract

Cx50 (connexin50), a member of the $\alpha$-family of gap junction proteins expressed in the lens of the eye, has been shown to be essential for normal lens development. In the present study, we identified a CaMBD [CaM (calmodulin)-binding domain] (residues 141–166) in the intracellular loop of Cx50. Elevations in intracellular $Ca^{2+}$ concentration effected a 95 % decline in $g_j$ (junctional conductance) of Cx50 in N2a cells that is likely to be mediated by CaM, because inclusion of the CaM inhibitor calmidazolium prevented this $Ca^{2+}$-dependent decrease in $g_j$. The direct involvement of the Cx50 CaMBD in this $Ca^{2+}$/CaM-dependent regulation was demonstrated further by the inclusion of a synthetic peptide encompassing the CaMBD in both whole-cell patch pipettes, which effectively prevented the intracellular $Ca^{2+}$-dependent decline in $g_j$. Biophysical studies using NMR and fluorescence spectroscopy reveal further that the peptide stoichiometrically binds to $Ca^{2+}$/CaM with an affinity of ~ 5 nM. The binding of the peptide expanded the $Ca^{2+}$-sensing range of CaM by increasing the $Ca^{2+}$ affinity of the C-lobe of CaM, while decreasing the $Ca^{2+}$ affinity of the N-lobe of CaM. Overall, these results demonstrate that the binding of $Ca^{2+}$/CaM to the intracellular loop of Cx50 is critical for mediating the $Ca^{2+}$-dependent inhibition of Cx50 gap junctions in the lens of the eye.

### Keywords

calcium; calmodulin; connexin50; gap junction; junctional conductance; protein–protein interaction

## INTRODUCTION

The circulation of current fluid flow through the closely packed cells of the lens of the eye is essential for lens homoeostasis, and is highly dependent on functional cell–cell coupling. This is accomplished by gap junctions, relatively non-selective channels that are permeable to low-molecular-mass (<1 kDa) molecules that directly link the cytoplasms of adjacent cells [1–3]. The gap junction channel formed between two adjacent cells comprises two



[1]To whom correspondence should be addressed (chejjy@langate.gsu.edu).

**AUTHOR CONTRIBUTION**

Jenny Yang, Charles Louis and Richard Veenstra conceived the project and designed experiments. Yanyi Chen, Yubin Zhou, Xianming Lin, Hing-Cheung Wong, Qin Xu and Jie Jiang collected and analysed data. Yanyi Chen, Jenny Yang, Charles Louis and Richard Veenstra wrote the paper with input from Yubin Zhou, Hing-Cheung Wong, Jie Jiang, Siming Wang and Monica Lurtz.

connexon hemichannels, one from each cell, joined in mirror symmetry. Each hemichannel is composed of six transmembrane Cx (connexin) proteins embedded in the plasma membrane of the cell. The mammalian lens comprises three different Cx proteins, namely Cx43, Cx46 and Cx50, that, like all other Cxs, have four transmembrane segments, a short N-terminal cytoplasmic region, one intracellular loop and two extracellular loops with a set of highly conserved cysteine residues; the major difference between all Cxs is in the sequences of their cytoplasmic loops and C-terminal tails [3].

Inhibition of cell–cell communication in lens by elevated $[Ca^{2+}]_i$ (intracellular $Ca^{2+}$ concentration) was first demonstrated as an increased internal electrical resistance [4] that was prevented by pre-incubation with CaM (calmodulin) antagonists. Elevated $[Ca^{2+}]_i$ also inhibits cell–cell communication in both bovine [5] and sheep [6] lens primary cell cultures. We have demonstrated that lens cell–cell communication was half-maximally inhibited at ~ 300 nM $[Ca^{2+}]_i$ [6] and was prevented by pre-incubation of lens cultures with CaM antagonists [7]. The rapid onset of this inhibition (within seconds) suggests that this is mediated by a direct interaction of CaM with one or more of the lens Cxs, rather than being mediated via the action of a CaM-dependent protein kinase. Indeed, Peracchia et al. [8] have demonstrated that CaM gates Cx32-containing gap junctions directly, and Török et al. [9] have identified two distinct CaM-binding amino acid sequences in Cx32, with the N- and C-lobes of CaM showing separate functions, suggesting *trans*-domain or *trans*-subunit bridging by CaM as a possible mechanism of gap junction gating [10]; notably, this CaM-binding motif in Cx32 is absent from the three lens Cxs.

To better understand the $Ca^{2+}$-dependent inhibition of lens gap junctions, we identified high-affinity CaM-binding sites in the lens Cxs Cx43 and Cx44 (the sheep homologue of human Cx46). Specifically, these domains encompass residues 138–157 in Cx43 [11] and residues 129–148 in Cx44 (corresponding to residues 138–157 in Cx46) [12]. These sequences have conserved hydrophobic residues at positions 1, 5, 10 and 14 that matched well with two major CaM-binding classes, 1–10 and 1–14, which are similar to the CaM-binding motifs found in calcineurin, nitric oxide synthase, adenylate cyclase and skeletal myosin light chain kinase [13,14]. These CaMBDs (CaM-binding domains) are located at the C-terminal end of the loop region between the predicted Cx TM (transmembrane region) 2 and TM3 [2–3,15–18] and are highly conserved in all three lens Cxs.

The present study was conducted to determine whether Cx50, like Cx43 and Cx44, was also regulated by $[Ca^{2+}]_i$ in the micromolar range, and, if so, whether this $Ca^{2+}$ regulation was CaM-mediated. A bioinformatic analysis [14] of Cx50 resulted in the identification of a candidate CaMBD with high predictive score that was located in the same C-terminal end of the loop region between the predicted Cx TM2 and TM3 of Cx50. This region is highly conserved in all three lens Cxs. A peptide model, which proved to be successful in our studies with Cx43 and Cx44 [11,12], was then adopted to demonstrate the physical contacts between the predicted Cx50 CaMBD and CaM. Studies using high-resolution NMR and fluorescence spectroscopy clearly established a high-affinity $Ca^{2+}$-dependent interaction between a domain in the intracellular loop of Cx50 and CaM. Our results provide important new insights into the molecular mechanism by which altered regulation of intracellular $Ca^{2+}$ concentration in the lens affects the regulation of lens Cx50 gap junctions.

## EXPERIMENTAL

### Prediction of transmembrane topology and a CaMBD

On the basis of a hidden Markov model, the topology and orientation of the transmembrane helices of the mouse Cx50 were predicted using four different programs, including TMHMM, MEMSAT, SOSUI and HMMTOP [16,19–21]. ClustalW2 was used to align

multiple mammalian gap junction polypeptide sequences in the $\alpha$-family, including Cx43 (GenBank® accession number NP_000156; Gja1 human), Cx44 (GenBank® accession number AAD56220; Gja3 sheep), Cx46 (GenBank® accession number NP_068773; Gja3 human) and Cx50 (GenBank® accession number AAF32309; Gja8 human). The candidate CaMBD in Cx50 was predicted using the CaM Target Database developed on the basis of over 100 known CaM target sequences [14].

## Peptides and proteins

The Cx50 peptide, Cx50p$^{141–166}$ ($S^{141}$SKGTKKFRLEGTLLRTYVCHIIFKT$^{166}$), was synthesized by EZ Biolab and purified by preparative reversed-phase HPLC with a purity of >87 %. A scrambled peptide, SCx50p (FKLYKCISFGGTEITTRSHVLTKKRL), with the same composition of amino acids which shows no predicted CaM-binding capacity, was synthesized with a purity of >90 % and served as a negative control. The molecular masses of these two peptides were determined by MALDI (matrix-assisted laser-desorption/ ionization)–TOF (time-of-flight)-MS in reflectron mode. To mimic the protein environment and remove extra charges, peptides were acylated at their N-termini and aminated at their C-termini.

Both $^{14}$N and $^{15}$N isotopically labelled recombinant rat CaMs were expressed and purified as described previously [11]. D-CaM (dansylated CaM) was prepared as described previously [22]. The concentration of CaM was determined using the $\varepsilon_{276}$ of 3030 $M^{-1} \cdot cm^{-1}$ [23]. The amount of dye bound was determined using an $\varepsilon_{335}$ of 3980 $M^{-1} \cdot cm^{-1}$ for D-CaM. The concentration of modified CaM was determined using the BCA (bicinchoninic acid) assay (Pierce) with BSA or unmodified CaM as the standard. The modification of CaM was confirmed further by MALDI–TOF-MS in the linear mode.

## Electrophysiological measurement of $g_j$ (junctional conductance)

Parental N2a cells were grown to 80 % confluence in a 12-well format and were transiently transfected with 1 $\mu$g of the pTracer-Cx50 cDNA plasmid for 4 h, lightly trypsinized and placed in 35-mm-diameter culture dishes overnight. Dual whole-cell patch-clamp experiments were performed the next day on GFP (green fluorescent protein)-expressing cell pairs to measure $g_j$, and the sensitivity to $[Ca^{2+}]_i$ was determined by permeabilizing the cells with 1 $\mu$M ionomycin and perfusing with ± 1.8 mM external $CaCl_2$ saline solutions. A +20 mV $V_j$ (transjunctional voltage) pulse was applied every 15 s to monitor $g_j$ during bath perfusion with nominally 0 or 1.8 mM $[Ca^{2+}]_o$ (external $Ca^{2+}$ concentration) saline solutions. The $g_j$ was normalized to the initial value ($G_j = g_j/g_{j,\,initial}$) for each Cx50 cell pair, and the results were pooled for each dataset. To examine the effect of CaM inhibitor or the candidate CaM-binding peptide on $g_j$, Cx50-N2a cells were pre-treated with 1 $\mu$M CDZ (calmidazolium) (Calbiochem) for 10–15 min or 1 $\mu$M of the synthetic Cx50 mimetic peptides (Cx50p$^{141–166}$ or SCx50p) were added to both whole-cell patch pipettes.

## NMR spectroscopy

NMR experiments were performed with a Varian INOVA 600 MHz NMR spectrometer at 37 °C. ($^1$H,$^{15}$N)-HSQC (heteronuclear single-quantum coherence) data were collected with 2048 complex data points and a spectral width of ~ 14 p.p.m. in the $^1$H dimension, and 128 increments and a spectral width of 33 p.p.m. in the $^{15}$N dimension. A sample of 0.26 mM uniformly $^{15}$N-labelled CaM in buffer consisting of 5 mM Mes, 10 mM Bis-Tris (pH 6.5), 5 mM DTT (dithiothreitol), 0.1 mM sodium azide, 10 mM $CaCl_2$ and 10 % $^2H_2O$ was titrated with peptide stock solutions (~ 5 mM) of the peptides Cx50p$^{141–166}$ or SCx50p in the same buffer. NMR data were processed using NMRPipe [24] and analysed using Sparky 3 (T.D. Goddard and D.G. Kneller, University of California, San Francisco).

The pulse-field gradient diffusion NMR spectra were collected with a modified PG-SLED pulse sequence [25] on a 600 MHz Varian INOVA spectrometer. In each FID (free induction decay) were contained 8k complex data points with a spectral width of ~ 13 p.p.m. The pulse-field gradient level ($G$) was arrayed from ~ 0.2 to ~ 31.0 Gauss/cm with a pulse gradient time ($\delta$) of 5 ms and a diffusion time ($\Delta$) of 112.5 ms. The data were processed using FELIX (Accelrys). The relationship between the NMR signal intensity ($A$) and the diffusion constant ($D$) follows eqn (1):

$$A=A_0\exp[-(\gamma\delta G^2)(\Delta-\delta/3)D] \quad (1)$$

where $A_0$ is the signal intensity when pulse gradient is not used and $\gamma$ is the gyromagnetic ratio of the proton. In the data processing, the signal intensity as a function of pulse-field gradient level was fitted with eqn (2) using KaleidaGraph 3.5 (Synergy). The values discussed in the present paper were all determined by fitting with a linear correlation coefficient ≥0.999.

$$A=A_0\exp(-CG^2) \quad (2)$$

where $C$ is a constant [ = $\gamma\delta(\Delta - \delta/3)D$], the diffusion constant and the hydrodynamic radii $R$ were obtained by comparing the $C$ values of different molecules measured under identical conditions using eqns (3) and (4):

$$D/D_0=C/C_0 \quad (3)$$

$$R/R_0=C_0/C \quad (4)$$

where $D_0$, $R_0$ and $C_0$ are the diffusion constant, hydrodynamic radius and the measured $C$ value of lysozyme. The hydrodynamic radius and diffusion constant of lysozyme have been reported previously [26]. The gradients were calibrated at 25 °C on the residual $^1$H signal in a sample of 99.9 % $^2H_2O$, using the published value of (1.902 ± 0.002) × $10^{-9}$ $m^2 \cdot s^{-1}$ for the self-diffusion coefficient of $^1H^2HO$ at 25 °C [27].

NMR samples contained 0.23 mM CaM in 10 % $^2H_2O$, 100 mM KCl and 10 mM imidazole at pH 6.5, with 10 mM $Ca^{2+}$ for $Ca^{2+}$-bound. The intensities of the protein signals were integrated from the methylene and methyl region of ~ 2 p.p.m. spectral width ( −0.2–1.8 p.p.m.). The integrated regions for each species were carefully selected to avoid or reduce interferences from buffer signals. The integrated intensities were normalized further to minimize the experimental errors from phase adjustment and baseline correction during the processing.

Chemical-shift perturbations ($\Delta$) of the ($^1$H,$^{15}$N)-HSQC spectra with and without peptide were calculated using both $^1$H and $^{15}$N chemical shifts ($\delta$) as shown in eqn (5):

$$\Delta\delta=\sqrt{\frac{(\Delta\delta^1\mathrm{H})^2+\left(\frac{\Delta\delta^{15}\mathrm{N}}{5}\right)^2}{2}} \quad (5)$$

## Fluorescence measurements

Steady-state fluorescence spectra were recorded using a QM1 fluorescence spectrophotometer (PTI) in a 1-cm-pathlength cell with a xenon short-arc lamp at 25 °C. The fluorescence emission spectra were acquired between 400 and 600 nm with an excitation

wavelength at 335 nm for D-CaM. The slit widths were set at 4 nm for excitation and 8 nm for emission. A solution (0.8 ml) containing 0.25–2 $\mu$M D-CaM in 10 mM Tris/HCl (pH 7.4) and 100 mM KCl, with 5 mM $Ca^{2+}$ or 5 mM EGTA was titrated by gradually adding 5–10 $\mu$l aliquots of the peptide stock solution (0.25–0.8 mM) in the same buffer. The binding constant of the synthetic peptide to modified CaM was obtained with a 1:1 binding model by fitting normalized florescence data as described previously [11,12].

The fluorescence anisotropy of D-CaM before and after addition of $Cx50p^{141–166}$ was measured with excitation at 335 nm and emission at 500 nm. An integration time of at least 20 s (20 points/s) was used to record the fluorescence signal, and all measurements were repeated at least three times by following established protocols [28,29].

Owing to domain-specific distribution of phenylalanine and tyrosine residues in CaM, the equilibrium $Ca^{2+}$-binding constants for CaM were determined by monitoring fluorescence of intrinsic phenylalanine ($\lambda_{ex}$ = 250 nm; $\lambda_{em}$ = 280 nm;) for N-domain or tyrosine ($\lambda_{ex}$ = 277 nm; $\lambda_{em}$ = 320) for C-domain at 25 °C as described previously [30]. For N- or C-domain $Ca^{2+}$-binding constants, 5–8 $\mu$M CaM was titrated with 5–10 $\mu$l aliquots of 50 or 15 mM $Ca^{2+}$ stock solution in $Ca^{2+}$ equilibrium buffer with 50 mM Hepes (pH 7.4), 100 mM KCl, 5 mM NTA (nitrilotriacetic acid) and 0.05 mM EGTA. The same method was applied for the 1:1 CaM/peptide mixture. Free $Ca^{2+}$ at each titration point was determined with the $Ca^{2+}$ dye Oregon Green 488 BAPTA-5N [5-nitro-1,2-bis-(*o*-aminophenoxy)ethane-*N,N,N′,N′*-tetra-acetic acid] (0.2 $\mu$M; $K_d$ = −21.7 ± 2.5 $\mu$M [12]) at an emission of 520 nm with excitation of 495 nm. The free concentration was obtained using eqn (6):

$$[Ca^{2+}]_{free} = K_d \frac{F - F_{min}}{F_{max} - F} \quad (6)$$

where $F$ is the fluorescence intensity of the dye at each titration point, $[Ca^{2+}]_{free}$ is the concentration of free ionized calcium in solution, and $F_{min}$ and $F_{max}$ represent the dye fluorescence intensities of $Ca^{2+}$-free form and $Ca^{2+}$-saturated dye respectively. The $Ca^{2+}$-binding affinity was obtained by fitting to the non-linear Hill equation:

$$f = \frac{[Ca^{2+}]_{free}^{h}}{K_d + [Ca^{2+}]_{free}^{h}} \quad (7)$$

where $f$ is the fractional change of intrinsic fluorescence intensity, $K_d$ is the $Ca^{2+}$ dissociation constant, and $h$ is the Hill coefficient.

## CD spectroscopy

CD spectra were recorded in the far-UV (190–260 nm) range on a Jasco-810 spectropolarimeter at ambient temperature (25 °C) using a 0.1-cm-pathlength quartz cuvette. The measurements of CaM and the CaM–$Cx50p^{141–166}$ complex (10 $\mu$M) were made in 10 mM Tris/HCl (pH 7.5) and 100 mM KCl with 5 mM $CaCl_2$ or 5 mM EGTA. All spectra presented were averaged for at least 15 scans, and the background signal from the buffer was removed from the sample signals. The far-UV CD spectra of the peptide in different percentages of TFE (trifluoroethanol) were obtained using a 20 $\mu$M concentration of $Cx50p^{141–166}$ in the same buffer. The secondary structures of the peptides were calculated with the online secondary-structure prediction server DICHROWEB [31]. The $\alpha$-helical content of peptides was predicted using the Agadir algorithm [32–34].

### Mass spectrometry

The MALDI–TOF-MS analysis was carried out on an Applied Biosystems 4800 plus MALDI–TOF/TOF analyser mass spectrometer. The data were acquired in a linear positive mode with SA (sinapinic acid) as matrix for CaM (50 $\mu$M) and the CaM–Cx50p$^{141–166}$ complex. The molecular mass of Cx50p$^{141–166}$ was also confirmed by MALDI–TOF-MS with CHCA ($\alpha$-cyano-4-hydroxycinnamic acid) as matrix. CaM (50 $\mu$M) and Cx50p$^{141–166}$ (50 $\mu$M) were mixed in 50 mM Tris/HCl (pH 7.5) and 100 mM KCl, and a 1 $\mu$l mixture was added with 10 $\mu$l of saturated SA solution and then dried on the MALDI plate for the measurement.

## RESULTS

### A putative CaMBD in the single cytoplasmic loop of Cx50

The CaM-binding site predication server, Calmodulin Target Database, was used to identify potential CaMBDs within Cx50, by taking into account the hydropathy, $\alpha$-helical propensity, residue mass, residue charge, hydrophobic residue content and helical class [14]. The highest predictive score was assigned to a stretch of sequences (residues 141–166; Figure 1) in the C-terminal portion of the intracellular loop of Cx50. Sequence alignments with previously characterized CaMBDs in rodent Cx43 [11] and sheep Cx44 (human Cx46) [12], and secondary-structure prediction, identified common features among the three $\alpha$-family Cxs that included: (i) the spacing of hydrophobic residues with bulky side chains, often used as anchor in CaM target complexes [35–37], followed a 1–5–10 pattern; (ii) all of the domains exhibited strict conservation in positions with positively charged residues, which help to drive the formation of CaM target complexes via electrostatic interactions [38]; and (iii) the CaMBDs were predicted to have a predominantly $\alpha$-helical structure. Helical wheel analysis further suggests the clustering of hydrophobic residues on one side and the frequent occurrence of charged residues on the opposite side. A peptide corresponding to the predicted CaMBD was subsequently synthesized for the functional and biophysical studies described below.

### $Ca^{2+}$-dependent uncoupling of Cx50 gap junctions requires CaM

To determine whether Cx50 gap junctions like those comprising Cx43 [11,39] and Cx46 [12] are regulated by $[Ca^{2+}]_i$, we first performed dual whole-cell patch-clamp experiments in Cx50-N2a cells. Perfusion with saline solution containing 1 $\mu$M ionomycin+1.8 mM $[Ca^{2+}]_o$ induced a time-dependent reduction in $G_j$ (Figure 2A and Table 1); we have shown previously that such treatment effects an elevation of $[Ca^{2+}]_i$ in HeLa cells [40]. Omission of 1.8 mM $CaCl_2$ from the bath saline prevented the Cx50 gap junction uncoupling response in the presence of 1 $\mu$M ionomycin.

To test whether the $Ca^{2+}$-dependent decrease in Cx50 $G_j$ produced by addition of 1 $\mu$M ionomycin+1.8 mM $[Ca^{2+}]_o$ required CaM, Cx50-N2a cell cultures were acutely (≤15 min) treated with CDZ (2 $\mu$M), a CaM inhibitor with a $K_d$ of ~ 1 $\mu$M [41]. Pre-treatment with CDZ prevented the $Ca^{2+}$-dependent decrease in $G_j$ (Figure 2B).

A more specific test for a role of Cx50 CaMBD in mediating the $Ca^{2+}$-dependent inhibition of this Cx was to add the 26-mer Cx50 mimetic peptide corresponding to residues 141–166 of the cytoplasmic loop to the Cx50-transfected N2A cells. A scrambled peptide containing a randomized sequence of the same amino acids was also utilized as a control. The addition of Cx50p$^{141–166}$, but not the scrambled peptide, prevented the decline in $G_j$ (Figure 2C). Overall, these electrophysiological data support the hypothesis that an elevation of $[Ca^{2+}]_i$ can uncouple Cx50 gap junctions in a CaM-dependent manner mediated by the Cx50 141–166 domain.

To examine the molecular basis for the $Ca^{2+}$-dependent decrease in Cx50 $G_j$, gap junction channel recordings were analysed in two poorly coupled cell pairs. Both experiments exhibited a maximum of three open channels ($N$) and their cumulative open probability ($N \cdot P_o$) declined from 1.21 open channels per unit time to 0 upon exposure to 1 $\mu$M ionomycin and 1.8 mM $[Ca^{2+}]_o$ saline (Figure 3A). Unitary Cx50 gap junction channel currents remained constant (314 ± 18 pS, mean ± S.D., $n = 14$) during the decline in $P_o$, indicative of a conformational gating type behaviour (Figure 3B).

## $Ca^{2+}$-dependent specific interaction between Cx50 CaMBD and CaM revealed by NMR

After confirming the requirement for CaM in the $Ca^{2+}$-dependent regulation of the Cx50 gap junctions, we further asked the question whether or not there is a direct interaction between the predicted CaMBD (or $Cx50p^{141–166}$) and CaM. The formation of the CaM–$Cx50p^{141–166}$ complex was first confirmed by MALDI–TOF-MS (see Supplementary Figure S1 at http://www.BiochemJ.org/bj/435/bj4350711add.htm). In the presence of $Ca^{2+}$, a distinct peak representing the CaM–$Cx50p^{141–166}$ complex (theoretical molecular mass 19.93 kDa; experimental molecular mass 20.02 kDa) was detected.

To identify residue-specific changes in the conformation of CaM during complex formation with $Cx50p^{141–166}$, we carried out ($^1H$,$^{15}N$)-HSQC NMR experiments. Unlabelled $Cx50p^{141–166}$ stock solution was gradually titrated into $^{15}N$-labelled CaM. Under $Ca^{2+}$-loaded conditions, the HSQC spectrum of $Ca^{2+}$-saturated CaM (holo-CaM) underwent significant changes on addition of 1 mol. eq. of $Cx50p^{141–166}$ (Figure 4A). In contrast, SCx50p, which is predicted to have no binding affinity for CaM, was similarly added to $^{15}N$-labelled holo-CaM. This scrambled peptide failed to induce chemical-shift changes in CaM (Figure 4B), therefore ruling out the possibility of non-specific interactions between peptide and CaM.

By analysing the NMR chemical shifts of CaM–peptide complexes deposited in the Biological Magnetic Resonance Bank (BMRB codes 1634, 4270, 5480, 5770, 5893, 5896, 15470 and 16465), we identified some significant changes in chemical shifts [$\delta$(CaM) − $\delta$(complex) > 1 S.D.] that are common to all complexes such as the $^1H$ shifts of $Ala^{57}$ and $Met^{71}$, and $^{15}N$ shift of $Ala^{128}$. In the classical CaM–CaMK ($Ca^{2+}$/CaM-dependent protein kinase) II$\alpha$ peptide structure with 1–10 binding mode, $Met^{71}$ and $Ala^{128}$ are in the hydrophobic pockets of CaM and are within 5 Å (1 Å = 0.1 nm) of the peptide. $Ala^{57}$ occupies the second position of the second $Ca^{2+}$-binding loop, suggesting that peptide binding leads to conformational change in this loop. In the CaM–$Cx50p^{141–166}$ complex, $Ala^{57}$ and $Met^{71}$ have $\delta_H$ values of 0.29 and 0.05 p.p.m. respectively, whereas $Ala^{128}$ has a $\delta_N$ of 0.21 p.p.m., consistent with $Cx50p^{141–166}$ bound to $Ca^{2+}$–CaM.

Upon the formation of a $Ca^{2+}$/CaM–$Cx50p^{141–166}$ complex, the most significant perturbations, with weighted average chemical shift changes greater than 0.1 p.p.m., were observed in the N-lobe (e.g. $Ser^{17}$, $Thr^{26}$, $Thr^{29}$, $Glu^{31}$, $Leu^{39}$ and $Ala^{57}$), the C-lobe (e.g. $Glu^{82}$, $Asp^{93}$, $Leu^{105}$, $Arg^{106}$, $Ala^{147}$ and $Lys^{148}$) and the linker region (e.g. $Asp^{64}$ and $Phe^{68}$), indicating that $Cx50p^{141–166}$ causes a global conformation changes in CaM. A detailed residue–residue plot of chemical-shift perturbation is shown in Figure 4(C). The overall change of the N-lobe residues (2.74 p.p.m.) was greater than in the C-lobe residues (1.78 p.p.m.). During the titration, we observed the simultaneous appearance of two peaks representing the same residue. For example, a progressive disappearance of the amide signal of $Gly^{33}$ representing unbound CaM was accompanied by the concomitant emergence of a new set of peaks from the CaM–$Cx50p^{141–166}$ complex (Figure 4D). Such a slow exchange process, which occurs when the exchange rate of the bound and unbound states is smaller than the amide frequency difference, often heralds a high affinity protein–protein or protein–peptide association (i.e. interactions with submicromolar affinities) [12,42].

### Probing the CaM–peptide complex state by diffusion NMR

Pulse-field gradient NMR was performed to determine the diffusion constant of the CaM–Cx50p$^{141–166}$ complex, enabling us to assess the overall size of this complex in solution. The diffusion constant was determined to be (12.4 ± 0.4) × $10^7$ cm/s (Figure 5). By assuming a spherical shape of the complex, the calculated size of the $Ca^{2+}$/CaM–Cx50p$^{141–166}$ complex was determined to be 17.3 ± 0.6 Å, a value comparable with the hydrodynamic radii of CaM in complex with well-known targets such as smMLCK (smooth muscle myosin light chain kinase) (17.9–21.8 Å), PDE (phosphodiesterase) (18.8–22.3Å) and CaMKI (21.2 Å) [43]. The hydrodynamic radius of CaM (22.6 ± 0.6 Å) was decreased by 23 % on formation of the CaM–Cx50p$^{141–166}$ complex. This size conforms to a collapsed structure of the complex that involves the unwinding of the central helix within CaM to embrace the target peptide.

### Revealing CaM–peptide interactions with CD spectroscopy

CD spectra also confirmed the structural and conformational changes during the formation of the CaM–Cx50p$^{141–166}$ complex. As indicated in Figure 6(A), the addition of Cx50p$^{141–166}$ to holo-CaM at a 1:1 molar ratio resulted in a ~ 6 %increase in the negative ellipticity at 222 nm. The hydrophobic environment in the peptide-binding pocket of holo-CaM could be the reason for the increase in the negative ellipticity attributed to the peptide itself. In contrast, a 5 % decrease at 222 nm and a 20 % decrease at 208 nm in the CD signal intensity were observed after the addition of Cx50p$^{141–166}$ to apo-CaM. Further exploring the interaction of apo-CaM with Cx50p$^{141–166}$ using NMR was not possible because of limited solubility of the peptide in 5 mM EGTA (see Supplementary Figure S2 at http://www.BiochemJ.org/bj/435/bj4350711add.htm).

We examined further the secondary structure of Cx50p$^{141–166}$ under different solvent conditions. TFE is known to induce $\alpha$-helical formation of peptides, and the helical content in the presence of TFE usually reflects its helical propensity [44]. Cx50p$^{141–166}$ becomes predominantly helical (>90 %) at TFE ≥30 % (v/v) (Figure 6B, inset), suggesting that the Cx50 CaM-binding sequence readily adopts an $\alpha$-helical configuration. Cx50, Cx44 and Cx43 exhibit 94, 55 and 33 % helical conformation respectively in the presence of 30 %TFE (Table 2).

The peptide in the absence of CaM has only 7 % $\alpha$-helix and 72 % random coil. The addition of peptide into CaM resulted in the addition of helicity as shown in Figure 6(A). Figure 6(C) shows that our difference CD spectrum of the CaM in the presence and absence of the peptide exhibits two negative minima at 208 and 222 nm. To understand the origin of the additional helicity due to the formation of the CaM–Cx50p$^{141–166}$ complex, we analysed the helical contents in the X-ray structure of $Ca^{2+}$-loaded calmodulin alone (PDB code 3CLN) and the complex structure of CaM–CaMKII peptide (PDB code 1CDM) since our chemical-shift studies suggest that CaM binds to Cx50p$^{141–166}$ in a similar binding mode as to the peptide of CaMKII (Figure 4E). CaM does not exhibit any additional change in its helical content upon formation of the complex with a helicity of ~ 62 %. Thus the complex-induced helicity is attributed to the conversion of peptide to be ~ 20 % helical.

### Determination of the CaM–peptide binding affinity by fluorescence spectroscopy

D-CaM has frequently been used to determine the binding affinity of the CaM–peptide interaction due to its sensitivity to the changes in the surrounding chemical environment and its ease of preparation [22]. The dansyl moiety has an emission maximum at ~ 500–510 nm, a range in which the signals from intrinsic aromatic residues are negligible. We first examined the dansyl fluorescence anisotropy changes to confirm the formation of complex in the low-micromolar range. Fluorescence anisotropy is dependent on the rotational

correlation time of fluorophore in the sample, and is often used to reflect the hydrodynamic properties of biomolecules [45]. The increase in anisotropy often arises from slower tumbling of the fluorophore and thus reports the formation of a larger complex. Indeed, upon addition of 1 mol. eq. of $Cx50p^{141–166}$, the anisotropy of the dansyl moiety within D-CaM increased from 0.083 to 0.125, suggesting the association of $Cx50p^{141–166}$ with $Ca^{2+}$–CaM (see Supplementary Figure S3 at http://www.BiochemJ.org/bj/435/bj4350711add.htm).

We then carried out the titration of peptide with D-CaM by monitoring the fluorescence emission between 400 and 600 nm. In the presence of $Ca^{2+}$, D-CaM showed a fluorescence maximum at 500 nm. With the addition of $Cx50p^{141–166}$, the dansyl fluorescence emission maximum blue-shifted to 474 nm with a concomitant enhancement of its fluorescence intensity (Figure 7A), implying that the dansyl group entered a more hydrophobic environment upon complex formation with peptide. In contrast, in the presence of EGTA (Figure 7B), although the dansyl fluorescence intensity also increased, the fluorescence maxima changed less than in the presence of $Ca^{2+}$. The data confirm the CD signal change on the addition of peptide to apo-CaM. By fitting the titration curve with a 1:1 binding mode, we obtained a $K_d$ of 4.9 ± 0.6 nM for the interaction between $Ca^{2+}$–CaM and $Cx50p^{141–166}$ (Table 2).

To investigate further the possible role of pH on CaM–peptide association, the effect of varying pH on the binding affinity of CaM for $Cx50p^{141–166}$ was also examined. As shown in Figure 7(C), the binding affinity (represented as $-\log K_d$) exhibited a pH-dependent change between pH 5.0 and 10.0. The highest binding affinity was obtained at pH 6.5. The observed pH-dependence of the interaction between CaM and $Cx50p^{141–166}$ indicates that electrostatic interactions are likely to be the main force driving CaM–peptide complex formation.

### Binding of $Cx50p^{141–166}$ expands the $[Ca^{2+}]_i$-sensing range of CaM

We next performed the $Ca^{2+}$ equilibrium titration of CaM to obtain macroscopic $Ca^{2+}$-binding constants for both the N- and C-lobes of CaM by monitoring domain-specific fluorescence changes as described previously [29,30]. The decrease in phenylalanine fluorescence ($\lambda_{ex}$ = 250 nm; $\lambda_{em}$ = 280 nm) and the increase in tyrosine fluorescence ($\lambda_{ex}$ = 277 nm; $\lambda_{em}$ = 320 nm) report $Ca^{2+}$ binding to the N-lobe and the C-lobe of CaM respectively. This allows us to examine the effect of peptide binding on the domain-specific $Ca^{2+}$-sensing capability of CaM. As shown in Figure 8 and summarized in Table 3, the addition of $Cx50p^{141–166}$ led to a rightward shift of the titration curve, representing the $Ca^{2+}$ binding to the N-lobe, and concomitantly caused a leftward shift of the titration curve, reflecting the $Ca^{2+}$ binding to the C-lobe of CaM. Specifically, the $Ca^{2+}$ affinity of the N-lobe of $Cx50p^{141–166}$-bound CaM decreased 2-fold, whereas the $Ca^{2+}$ affinity of the C-lobe increased by ~ 20 %. As a result of $Cx50p^{141–166}$ binding, CaM responded to subtle changes in $[Ca^{2+}]_i$ over a broader range of calcium concentrations.

## DISCUSSION

### Regulation of Cxs by intracellular $Ca^{2+}$ and CaM

The results of the present study demonstrate that intracellular calcium is important in the regulation of Cx50 gap junctions [40]. Furthermore, using the CaM inhibitor CDZ as well as a peptide fragment encompassing the predicted CaM-binding region, we were able to demonstrate that this $Ca^{2+}$-dependent inhibition of Cx50 gap junctions is mediated by the ubiquitous intracellular $Ca^{2+}$ receptor CaM. Thus CaM appears to mediate the $Ca^{2+}$-dependent regulation of all three major $\alpha$-Cxs in the lens, i.e. Cx43, Cx46 and Cx50. Our results also demonstrate that this inhibition of Cx50 gap junction channels by $Ca^{2+}$ is due to

a decrease in channel open time probability as opposed to a reduction in single-channel conductance (Figure 3A). These records provide the first direct evidence for the gated closure of individual Cx gap junction channels by $Ca^{2+}$–CaM. The average observed $g_j$ value of 314 pS is indicative of Cx50, since it is at least double the observed $g_j$ for Cx40, Cx43 or Cx45 gap junctions in our Cx50-N2a cell cultures and consistent with the reported 210–290 pS values from reconstituted lens fibre cell membranes or exogenously expressed Cx50 gap junction channels ([46–50], and Q. Xu, Y. Chen, J.J. Yang and R.D. Veenstra, unpublished work).

The possible role of CaM in the chemical gating of the $\beta$-family Cxs was first proposed by Peracchia and Wang [51]. CaM co-localizes with Cx32 [9] and directly gates Cx32-containing gap junctions [52]. Török et al. [9] reported that fluorescently labelled CaM derivatives bind to synthetic peptides spanning most of the cytoplasmic sequences from two regions of Cx32: an N-terminal sequence comprising residues 1–21 ($K_d$ = 27 nM) or residues 1–19 ($K_d$ = 1.1 $\mu$M); and a C-terminal sequence comprising residues 216–230 ($K_d$ = 2.1 $\mu$M) or residues 208–226 ($K_d$ = 3.5 $\mu$M). Both exhibit $Ca^{2+}$-dependent CaM-binding properties [9,10]. They also identified two distinct CaM-binding amino acid sequences in Cx32 within the N- and C-lobes of CaM showing separate functions, suggesting *trans*-domain or *trans*-subunit bridging by CaM as a possible mechanism of gap junction gating [52]. In addition, Ahmad et al. [53] using in *vitro* translation approaches have shown that oligomerization of Cx32 is CaM-dependent, since CaM interacts with Cxs at an early stage of gap junction assembly [8,9]. The C-terminal tail of the CaM-binding site of Cx32 is likely to be involved in the assembly of Cxs and is $Ca^{2+}$-dependent [8]. Furthermore, Blodow et al. [54] reported that CaM antagonists suppress gap junction coupling of Cx26 in isolated Hensen cells of the guinea pig cochlea. Taken together, $[Ca^{2+}]_i$ and CaM play vital roles in regulating gap junctions mediated by both the $\alpha$- and $\beta$-family of Cxs.

### Comparison of CaM-binding affinity with the α-family Cxs

Using high-resolution NMR, CD and fluorescence studies, we have shown using a peptide model that CaM interacts with the predicted cytosolic CaMBD of Cx50. Our current studies, as well as previous studies, have clearly shown that CaM exhibits a $Ca^{2+}$-dependent interaction of all three peptide fragments encompassing the intracellular loop regions of all three lens Cxs. Fluorescence spectroscopy revealed conformational changes of both the peptide and CaM following formation of the CaM–peptide complex. NMR studies demonstrated that the peptide binds to CaM with a 1:1 stoichiometry. It also indicated that the peptide induces structural changes in both the N- and C-terminal domains, as well as in the linker region of CaM and the binding of Cx peptides to CaM reflects a classical embracing mode of interaction. Overall, for these three Cxs, binding of the peptide to CaM decreases the apparent $K_d$ of $Ca^{2+}$ for CaM, and the Hill coefficient increased. In addition, Cx43 exhibits weaker affinity for CaM than does either Cx50 or Cx44.

Consistent with the CaM–Cx peptide binding affinity studies using fluorescence spectroscopy, our NMR chemical-shift analysis also supports a lower affinity for the CaM–$Cx43p^{136–158}$ complex. The addition of $Cx43p^{136–158}$ and $Cx50p^{141–166}$ results in similar changes in the CaM spectra as shown in Supplementary Figure S4 (at http://www.BiochemJ.org/bj/435/bj4350711add.htm). For most signals, the directionalities of the changes are the same, reflecting the same 1–5–10 binding mode of these peptides to CaM. However, we have observed the slow exchange process for $Gly^{33}$ in Cx50 shown in Figure 4(D). A similar scenario was observed for $Thr^{29}$, $Ala^{57}$ and $Thr^{117}$ for the CaM–$Cx44p^{129–150}$ complex [12]. Such a slow exchange process occurs when the exchange rate of the bound and unbound states is smaller than the amide frequency difference, and often heralds a high-affinity protein–protein or protein–peptide association (i.e. interactions with submicromolar affinities) [42] that is consistent with the CaM-binding affinity to

Cx50p$^{141–166}$ and Cx44p$^{129–150}$. In contrast, the NMR signals of CaM upon addition of Cx43p$^{136–158}$ exhibits a gradual change in chemical shifts characteristic of the fast exchange regime, suggesting a weaker binding affinity.

### Implications for the factors contributing to the CaM-binding affinity to Cxs

There are several positively charged residues, such as Lys$^{147}$, Arg$^{149}$ and Arg$^{156}$, in Cx50 that are conserved in all $\alpha$-family members. To identify the key factors responsible for the binding affinity of CaM to Cxs, we have determined the CaM-binding affinity of Cx50p$^{141–166}$ to CaM as a function of pH. The peptide-binding affinity is decreased at pH values lower than 5.5 and greater than 8.5. This trend is very similar to our previous results reported for Cx44 [12]. Both Cx44p$^{129–150}$ and Cx50p$^{141–166}$ behave similarly when pH is varied, but CaM binding to Cx50p$^{141–166}$ is ~ 1 order of magnitude stronger than to the Cx44p$^{129–150}$. Such a similar pH-dependence suggests that electrostatic interactions following the protonation of aspartate and glutamate and deprotonation of lysine are important for this complex formation.

The difference in CaM-binding affinity of Cx50p$^{141–166}$ and Cx44p$^{129–150}$ may originate from the intrinsic sequences encoded in the CaM-binding regions of different Cxs. As shown in Figure 1, there are several differences in the predicted regions especially with variations between conserved residue positions 1 and 5. Cx43 contains two flexible glycine residues instead of the helix-forming residues in Cx44 and Cx50. Such sequence variation reflects their ability to form $\alpha$-helices that are important for their interaction with CaM [14]. As shown in Figure 6(B) and Table 2, Cx43p$^{136–158}$ has the lowest $\alpha$-helix-formation capacity. The addition of TFE (>60 %) induces the highest $\alpha$-helical content in the Cx50p$^{141–166}$ and Cx44p$^{129–150}$. In Figure 6(B), the $\alpha$-helicity of Cx50p$^{141–166}$ is higher than that of Cx43p$^{136–158}$ and Cx44p$^{129–150}$ reported previously [11,12]. The calculated $\alpha$-helical content of peptides in TFE exhibits the rank order Cx50p$^{141–166}$>Cx44p$^{129–150}$>Cx43p$^{136–158}$. Interestingly, negatively charged Glu$^{151}$ located close to Arg$^{149}$ in Cx50 may stabilize the $\alpha$-helical conformation of this peptide. In contrast, Cx43 has a positively charged arginine residue at the same location that may disable $\alpha$-helical conformation. The $\alpha$-helical content of the CaM-binding peptides observed is consistent with the trend for the CaM-binding affinity results from our fluorescence experiments (Table 2). Both Cx44 and Cx50p$^{141–166}$ also bind CaM in the absence of $Ca^{2+}$, as revealed by fluorescence data. The CaM-binding affinities to Cx44 and Cx50 in EGTA are 100- and 1000-fold weaker than those in the presence of $Ca^{2+}$ respectively. The apo-form of CaM does not interact with Cx43p$^{136–158}$, which has the least $\alpha$-helical content. Therefore our results reveal that the $\alpha$-helicity of the CaM-binding peptide is an important factor in predicting the CaM-binding affinity of these Cxs.

Our detailed NMR analysis has also revealed the differential interactions of CaM with Cx50p$^{141–166}$ and Cx43p$^{136–158}$. We observed that, in general, the N-lobe of CaM–Cx50p$^{141–166}$ has larger chemical-shift changes, whereas the C-lobe has smaller changes than those of CaM–Cx43p$^{136–158}$, although such interactions belong to a similar 1–5–10 binding mode. In addition, chemical shifts of residues such as Phe$^{12}$, Lys$^{13}$, Lys$^{94}$, Leu$^{116}$, Ile$^{130}$ and Met$^{145}$ of CaM–Cx50p$^{141–166}$ changed in different directions compared with those of CaM–Cx43p$^{136–158}$ (see Supplementary Figure S4). Among these residues, Lys$^{94}$ and Ile$^{130}$ are on the third and fourth $Ca^{2+}$-binding loops respectively, and these loops could be flexible and adopt different conformations, leading to different directions of change in chemical shifts. In the structure of CaM–CaMKII$\alpha$ (PDB code 1CDM), Leu$^{116}$ interacts with Lys$^{298}$, which corresponds to Lys$^{146}$ in Cx43 and Arg$^{149}$ in Cx50. Similarly, Met$^{145}$ interacts with Lys$^{300}$, which corresponds to Arg$^{148}$ in Cx43 and Glu$^{151}$ in Cx50 (Figure 4E). Such changes in directions of the chemical shifts of CaM are likely to be due to the intrinsic

properties such as the α-helical propensity of the sequences in the CaM-binding regions of Cxs.

## Structural and disease implications

The intracellular region regulated by CaM has been reported to be involved in several disease-related mutations. ODDD (oculodentodigital dysplasia) is caused by mutations in Cx43 such as G138R, G138S, G143S, G143D, K144E, V145G, M147T, R148G, R1481, T154A and T154N [55], overlapping with the CaM-binding region identified previously [11]. There have been no reports of point mutations in the CaMBD of Cx50 associated with cataract formation. However, Beahm and Hall [56] have reported that the Cx50 H161N mutant does not form detectable hemichannels, but forms gap junctions indistinguishable from wild-type. Interestingly, Toloue et al. [57] identified three nonfunctional mutations in Cx50, T157C, H161C and E169C, that failed to function homotypically or in heterotypic pairings with wild-type Cx50. The threonine residue at position 157 is highly conserved and this residue has been shown previously to be functionally essential for all Cxs tested, including Cx26, Cx43 and Cx50 [58]. Mutation of a conserved threonine residue in the third transmembrane helix of α- and β-Cxs creates a dominant-negative closed gap junction channel [58]. It is possible that such mutations may compromise the regulation of this Cx by CaM. The testing of such mutational effect on Cx50 function is currently underway in this laboratory.

The molecular scenario of CaM-mediated regulation of the α-class of gap junctions seems to be quite different from the β-class, probably due to the fact that the α-class Cxs lack the N-terminal glycine hinge and possess longer intracellular loops and C-termini than the β-class Cxs. Indeed, the CaM-targeting sequences in the α-class Cxs, such as rodent Cx43, sheep Cx44 (or human Cx46) and mouse Cx50, as revealed in the present study, are in the cytoplasmic loop connecting TM2 and TM3, in close proximity to the cytoplasmic loop–TM3 interface. The apparent juxtaposition of the Cx32 N-terminal CaMBD to TM1 and of the Cx43 cytoplasmic loop CaMBD to TM3 may facilitate the closing of the Cx channel pore since both TM1 and TM3 are suggested to be involved in forming the transmembrane pore while the N-terminus loops back to form a pore cytoplasmic vestibule.

The recently determined three-dimensional structure of the Cx26 gap junction channel at 3.5 Å resolution provides insights into the gating mechanism of the β-class of gap junctions at atomic resolution [59]. In this tsuzumi (Japanese drum)-shaped structure, the permeation pathway is mainly defined by the short NTH (N-terminal helix) (residues 2–10) that lines the pore funnel of gap junction channel and TM1 that constitutes the pore-lining helix. This structure suggests that the molecular identity of the channel ‘plug’ observed using electron microscopy [60] is likely to be the NTH. However, owing to the invisibility of both the cytoplasmic loop and the C-terminus in the crystal structure, both of which play important roles in the chemical gating of gap junctions [61], it is still too premature to explain the chemical gating mechanism with the current structure.

Given that the N-terminal CaMBD in Cx32 overlaps with the NTH that is believed to form the channel ‘plug’ in β-class gap junctions, it is conceivable that the $Ca^{2+}$-dependent binding of CaM to NTH might function as ‘cork’ to block the channel by the complex or by inducing conformational changes in the NTH. However, since the NTH is lined interior to the channel to form a funnel, its accessibility to CaM in the assembled channel remains to be confirmed.

Despite the absence of X-ray structural information about the intracellular loop of Cxs [59], we have provided detailed structural information about the association of CaM with all three α-family Cx members. Our results provide the first direct evidence that CaM binds to a specific region of the lens gap junction Cxs Cx43, Cx44 and Cx50 in a $Ca^{2+}$-dependent

manner [11,12]. Our data suggest a common conformational gating mechanism by which the $Ca^{2+}$-dependent inhibition of the $\alpha$-class of gap junction proteins is mediated by the direct association of an intracellular loop region of these proteins with $Ca^{2+}$–CaM [6,7,39,40].

## Supplementary Material

Refer to Web version on PubMed Central for supplementary material.

## Acknowledgments

**FUNDING**

This work is supported in part by the National Institutes of Health [grant numbers EY-05684 (to C.F.L. and J.J.Y.), HL-042220 (to R.D.V.) and GM-081749 (to J.J.Y.)].

## Abbreviations used

| | |
|---|---|
| **BAPTA-5N** | 5-nitro-1,2-bis-(*o*-aminophenoxy)ethane-*N*,*N*,*N*′,*N*′-tetra-acetic acid |
| **$[Ca^{2+}]_i$** | intracellular $Ca^{2+}$ concentration |
| **$[Ca^{2+}]_o$** | external $Ca^{2+}$ concentration |
| **CaM** | calmodulin |
| **apo-CaM** | $Ca^{2+}$-chelated CaM |
| **D-CaM** | dansylated CaM |
| **holo-CaM** | $Ca^{2+}$-saturated CaM |
| **CaMBD** | CaM-binding domain |
| **CaMK** | $Ca^{2+}$/CaM-dependent protein kinase |
| **CDZ** | calmidazolium |
| **CHCA** | $\alpha$-cyano-4-hydroxycinnamic acid |
| **Cx** | connexin |
| **DTT** | dithiothreitol |
| **$g_j$** | junctional conductance |
| **HSQC** | heteronuclear single-quantum coherence |
| **MALDI** | matrix-assisted laser-desorption/ionization |
| **NTA** | nitrilotriacetic acid |
| **NTH** | N-terminal helix |
| **SA** | sinapinic acid |
| **TFE** | trifluoroethanol |
| **TM** | transmembrane region |
| **TOF** | time-of-flight |
| **$V_j$** | transjunctional voltage |

## References


1. Bruzzone R, White TW, Paul DL. Connections with connexins: the molecular basis of direct intercellular signaling. Eur J Biochem. 1996; 238:1–27. [PubMed: 8665925]
2. Evans WH, Martin PE. Gap junctions: structure and function. Mol Membr Biol. 2002; 19:121–136. [PubMed: 12126230]
3. Willecke K, Eiberger J, Degen J, Eckardt D, Romualdi A, Guldenagel M, Deutsch U, Sohl G. Structural and functional diversity of connexin genes in the mouse and human genome. Biol Chem. 2002; 383:725–737. [PubMed: 12108537]
4. Gandolfi SA, Duncan G, Tomlinson J, Maraini G. Mammalian lens inter-fiber resistance is modulated by calcium and calmodulin. Curr Eye Res. 1990; 9:533–541. [PubMed: 2387165]
5. Crow JM, Atkinson MM, Johnson RG. Micromolar levels of intracellular calcium reduce gap junctional permeability in lens cultures. Invest Ophthalmol Visual Sci. 1994; 35:3332–3341. [PubMed: 8045723]
6. Churchill GC, Lurtz MM, Louis CF. $Ca^{2+}$ regulation of gap junctional coupling in lens epithelial cells. Am J Physiol Cell Physiol. 2001; 281:C972–C981. [PubMed: 11502574]
7. Lurtz MM, Louis CF. Calmodulin and protein kinase C regulate gap junctional coupling in lens epithelial cells. Am J Physiol Cell Physiol. 2003; 285:C1475–C1482. [PubMed: 12917107]
8. Peracchia C, Sotkis A, Wang XG, Peracchia LL, Persechini A. Calmodulin directly gates gap junction channels. J Biol Chem. 2000; 275:26220–26224. [PubMed: 10852921]
9. Török K, Stauffer K, Evans WH. Connexin 32 of gap junctions contains two cytoplasmic calmodulin-binding domains. Biochem J. 1997; 326:479–483. [PubMed: 9291121]
10. Dodd R, Peracchia C, Stolady D, Török K. Calmodulin association with connexin32-derived peptides suggests *trans*-domain interaction in chemical gating of gap junction channels. J Biol Chem. 2008; 283:26911–26920. [PubMed: 18676375]
11. Zhou Y, Yang W, Lurtz MM, Ye Y, Huang Y, Lee HW, Chen Y, Louis CF, Yang JJ. Identification of the calmodulin binding domain of connexin 43. J Biol Chem. 2007; 282:35005–35017. [PubMed: 17901047]
12. Zhou Y, Yang W, Lurtz MM, Chen Y, Jiang J, Huang Y, Louis CF, Yang JJ. Calmodulin mediates the $Ca^{2+}$-dependent regulation of Cx44 gap junctions. Biophys J. 2009; 96:2832–2848. [PubMed: 19348766]
13. O'Day DH. CaMBOT: profiling and characterizing calmodulin-binding proteins. Cell Signalling. 2003; 15:347–354. [PubMed: 12618209]
14. Yap KL, Kim J, Truong K, Sherman M, Yuan T, Ikura M. Calmodulin target database. J Struct Funct Genomics. 2000; 1:8–14. [PubMed: 12836676]
15. Jones DT, Taylor WR, Thornton JM. A model recognition approach to the prediction of all-helical membrane protein structure and topology. Biochemistry. 1994; 33:3038–3049. [PubMed: 8130217]
16. Krogh A, Larsson B, von Heijne G, Sonnhammer EL. Predicting transmembrane protein topology with a hidden Markov model: application to complete genomes. J Mol Biol. 2001; 305:567–580. [PubMed: 11152613]
17. Tusnady GE, Simon I. Principles governing amino acid composition of integral membrane proteins: application to topology prediction. J Mol Biol. 1998; 283:489–506. [PubMed: 9769220]
18. Hofmann K, Stoffel W. TMbase: a database of membrane spanning protein segments. Biol Chem Hoppe-Seyler. 1993; 374:166.
19. Mitaku S, Hirokawa T, Tsuji T. Amphiphilicity index of polar amino acids as an aid in the characterization of amino acid preference at membrane–water interfaces. Bioinformatics. 2002; 18:608–616. [PubMed: 12016058]
20. Jones DT. Do transmembrane protein superfolds exist? FEBS Lett. 1998; 423:281–285. [PubMed: 9515724]
21. Tusnady GE, Simon I. The HMMTOP transmembrane topology prediction server. Bioinformatics. 2001; 17:849–850. [PubMed: 11590105]
22. Johnson JD, Wittenauer LA. A fluorescent calmodulin that reports the binding of hydrophobic inhibitory ligands. Biochem J. 1983; 211:473–479. [PubMed: 6870843]

23. Wallace RW, Tallant EA, Cheung WY. Assay of calmodulin by $Ca^{2+}$-dependent phosphodiesterase. Methods Enzymol. 1983; 102:39–47. [PubMed: 6316081]
24. Delaglio F, Grzesiek S, Vuister GW, Zhu G, Pfeifer J, Bax A. NMRPipe: a multidimensional spectral processing system based on UNIX pipes. J Biomol NMR. 1995; 6:277–293. [PubMed: 8520220]
25. Wilkins DK, Grimshaw SB, Receveur V, Dobson CM, Jones JA, Smith LJ. Hydrodynamic radii of native and denatured proteins measured by pulse field gradient NMR techniques. Biochemistry. 1999; 38:16424–16431. [PubMed: 10600103]
26. Lee HW, Yang W, Ye Y, Liu ZR, Glushka J, Yang JJ. Isolated EF-loop III of calmodulin in a scaffold protein remains unpaired in solution using pulsed-field-gradient NMR spectroscopy. Biochim Biophys Acta. 2002; 1598:80–87. [PubMed: 12147347]
27. Mills R. Self-diffusion in normal and heavy water in the range 1–45°. J Phys Chem. 1973; 77:685–688.
28. LaPorte DC, Keller CH, Olwin BB, Storm DR. Preparation of a fluorescent-labeled derivative of calmodulin which retains its affinity for calmodulin binding proteins. Biochemistry. 1981; 20:3965–3972. [PubMed: 6269577]
29. Theoharis NT, Sorensen BR, Theisen-Toupal J, Shea MA. The neuronal voltage-dependent sodium channel type II IQ motif lowers the calcium affinity of the C-domain of calmodulin. Biochemistry. 2008; 47:112–123. [PubMed: 18067319]
30. VanScyoc WS, Sorensen BR, Rusinova E, Laws WR, Ross JB, Shea MA. Calcium binding to calmodulin mutants monitored by domain-specific intrinsic phenylalanine and tyrosine fluorescence. Biophys J. 2002; 83:2767–2780. [PubMed: 12414709]
31. Whitmore L, Wallace BA. DICHROWEB, an online server for protein secondary structure analyses from circular dichroism spectroscopic data. Nucleic Acids Res. 2004; 32:W668–W673. [PubMed: 15215473]
32. Munoz V, Serrano L. Elucidating the folding problem of helical peptides using empirical parameters. II Helix macrodipole effects and rational modification of the helical content of natural peptides. J Mol Biol. 1995; 245:275–296. [PubMed: 7844817]
33. Munoz V, Serrano L. Elucidating the folding problem of helical peptides using empirical parameters. III Temperature and pH dependence. J Mol Biol. 1995; 245:297–308. [PubMed: 7844818]
34. Munoz V, Serrano L. Elucidating the folding problem of helical peptides using empirical parameters. Nat Struct Biol. 1994; 1:399–409. [PubMed: 7664054]
35. Nicol S, Rahman D, Baines AJ. $Ca^{2+}$-dependent interaction with calmodulin is conserved in the synapsin family: identification of a high-affinity site. Biochemistry. 1997; 36:11487–11495. [PubMed: 9298969]
36. Yamauchi E, Nakatsu T, Matsubara M, Kato H, Taniguchi H. Crystal structure of a MARCKS peptide containing the calmodulin-binding domain in complex with $Ca^{2+}$–calmodulin. Nat Struct Biol. 2003; 10:226–231. [PubMed: 12577052]
37. Meador WE, Means AR, Quiocho FA. Modulation of calmodulin plasticity in molecular recognition on the basis of X-ray structures. Science. 1993; 262:1718–1721. [PubMed: 8259515]
38. Andre I, Kesvatera T, Jonsson B, Akerfeldt KS, Linse S. The role of electrostatic interactions in calmodulin–peptide complex formation. Biophys J. 2004; 87:1929–1938. [PubMed: 15345569]
39. Lurtz MM, Louis CF. Intracellular calcium regulation of connexin43. Am J Physiol Cell Physiol. 2007; 293:C1806–C1813. [PubMed: 17898133]
40. Yang DI, Louis CF. Molecular cloning of ovine connexin44 and temporal expression of gap junction proteins in a lens cell culture. Invest Ophthalmol Visual Sci. 2000; 41:2658–2664. [PubMed: 10937579]
41. Illiano S, Nagao T, Vanhoutte PM. Calmidazolium, a calmodulin inhibitor, inhibits endothelium-dependent relaxations resistant to nitro-L-arginine in the canine coronary artery. Br J Pharmacol. 1992; 107:387–392. [PubMed: 1358391]
42. Fielding L. NMR methods for the determination of protein–ligand dissociation constants. Curr Top Med Chem. 2003; 3:39–53. [PubMed: 12577990]

43. Weljie AM, Yamniuk AP, Yoshino H, Izumi Y, Vogel HJ. Protein conformational changes studied by diffusion NMR spectroscopy: application to helix–loop–helix calcium binding proteins. Protein Sci. 2003; 12:228–236. [PubMed: 12538886]
44. Yang JJ, Buck M, Pitkeathly M, Kotik M, Haynie DT, Dobson CM, Radford SE. Conformational properties of four peptides spanning the sequence of hen lysozyme. J Mol Biol. 1995; 252:483–491. [PubMed: 7563067]
45. Ludescher RD, Johnson ID, Volwerk JJ, de Haas GH, Jost PC, Hudson BS. Rotational dynamics of the single tryptophan of porcine pancreatic phospholipase $A_2$, its zymogen, and an enzyme/micelle complex: a steady-state and time-resolved anisotropy study. Biochemistry. 1988; 27:6618–6628. [PubMed: 3219357]
46. Veenstra RD, Wang HZ, Beyer EC, Brink PR. Selective dye and ionic permeability of gap junction channels formed by connexin45. Circ Res. 1994; 75:483–490. [PubMed: 7520372]
47. Beblo DA, Wang HZ, Beyer EC, Westphale EM, Veenstra RD. Unique conductance, gating, and selective permeability properties of gap junction channels formed by connexin40. Circ Res. 1995; 77:813–822. [PubMed: 7554128]
48. Donaldson P, Kistler J. Reconstitution of channels from preparations enriched in lens gap junction protein MP70. J Membr Biol. 1992; 129:155–165. [PubMed: 1279178]
49. Srinivas M, Costa M, Gao Y, Fort A, Fishman GI, Spray DC. Voltage dependence of macroscopic and unitary currents of gap junction channels formed by mouse connexin50 expressed in rat neuroblastoma cells. J Physiol. 1999; 517:673–689. [PubMed: 10358109]
50. Xu X, Berthoud VM, Beyer EC, Ebihara L. Functional role of the carboxyl terminal domain of human connexin 50 in gap junctional channels. J Membr Biol. 2002; 186:101–112. [PubMed: 11944087]
51. Peracchia C, Wang XC. Connexin domains relevant to the chemical gating of gap junction channels. Braz J Med Biol Res. 1997; 30:577–590. [PubMed: 9283624]
52. Dodd R, Peracchia C, Stolady D, Török K. Calmodulin association with connexin32-derived peptides suggests *trans*-domain interaction in chemical gating of gap junction channels. J Biol Chem. 2008; 283:26911–26920. [PubMed: 18676375]
53. Ahmad S, Martin PE, Evans WH. Assembly of gap junction channels: mechanism, effects of calmodulin antagonists and identification of connexin oligomerization determinants. Eur J Biochem. 2001; 268:4544–4552. [PubMed: 11502216]
54. Blodow A, Ngezahayo A, Ernst A, Kolb HA. Calmodulin antagonists suppress gap junction coupling in isolated Hensen cells of the guinea pig cochlea. Pflügers Arch. 2003; 446:36–41.
55. Paznekas WA, Karczeski B, Vermeer S, Lowry RB, Delatycki M, Laurence F, Koivisto PA, Van Maldergem L, Boyadjiev SA, Bodurtha JN, Jabs EW. *GJA1* mutations, variants, and connexin 43 dysfunction as it relates to the oculodentodigital dysplasia phenotype. Hum Mutat. 2009; 30:724–733. [PubMed: 19338053]
56. Beahm DL, Hall JE. Hemichannel and junctional properties of connexin 50. Biophys J. 2002; 82:2016–2031. [PubMed: 11916859]
57. Toloue MM, Woolwine Y, Karcz JA, Kasperek EM, Nicholson BJ, Skerett IM. Site-directed mutagenesis reveals putative regions of protein interaction within the transmembrane domains of connexins. Cell Commun Adhes. 2008; 15:95–105. [PubMed: 18649182]
58. Beahm DL, Oshima A, Gaietta GM, Hand GM, Smock AE, Zucker SN, Toloue MM, Chandrasekhar A, Nicholson BJ, Sosinsky GE. Mutation of a conserved threonine in the third transmembrane helix of $\alpha$- and $\beta$-connexins creates a dominant-negative closed gap junction channel. J Biol Chem. 2006; 281:7994–8009. [PubMed: 16407179]
59. Maeda S, Nakagawa S, Suga M, Yamashita E, Oshima A, Fujiyoshi Y, Tsukihara T. Structure of the connexin 26 gap junction channel at 3.5 Å resolution. Nature. 2009; 458:597–602. [PubMed: 19340074]
60. Oshima A, Tani K, Hiroaki Y, Fujiyoshi Y, Sosinsky GE. Three-dimensional structure of a human connexin26 gap junction channel reveals a plug in the vestibule. Proc Natl Acad Sci USA. 2007; 104:10034–10039. [PubMed: 17551008]
61. Peracchia C, Wang XG, Peracchia LL. Chemical gating of gap junction channels. Methods. 2000; 20:188–195. [PubMed: 10671312]

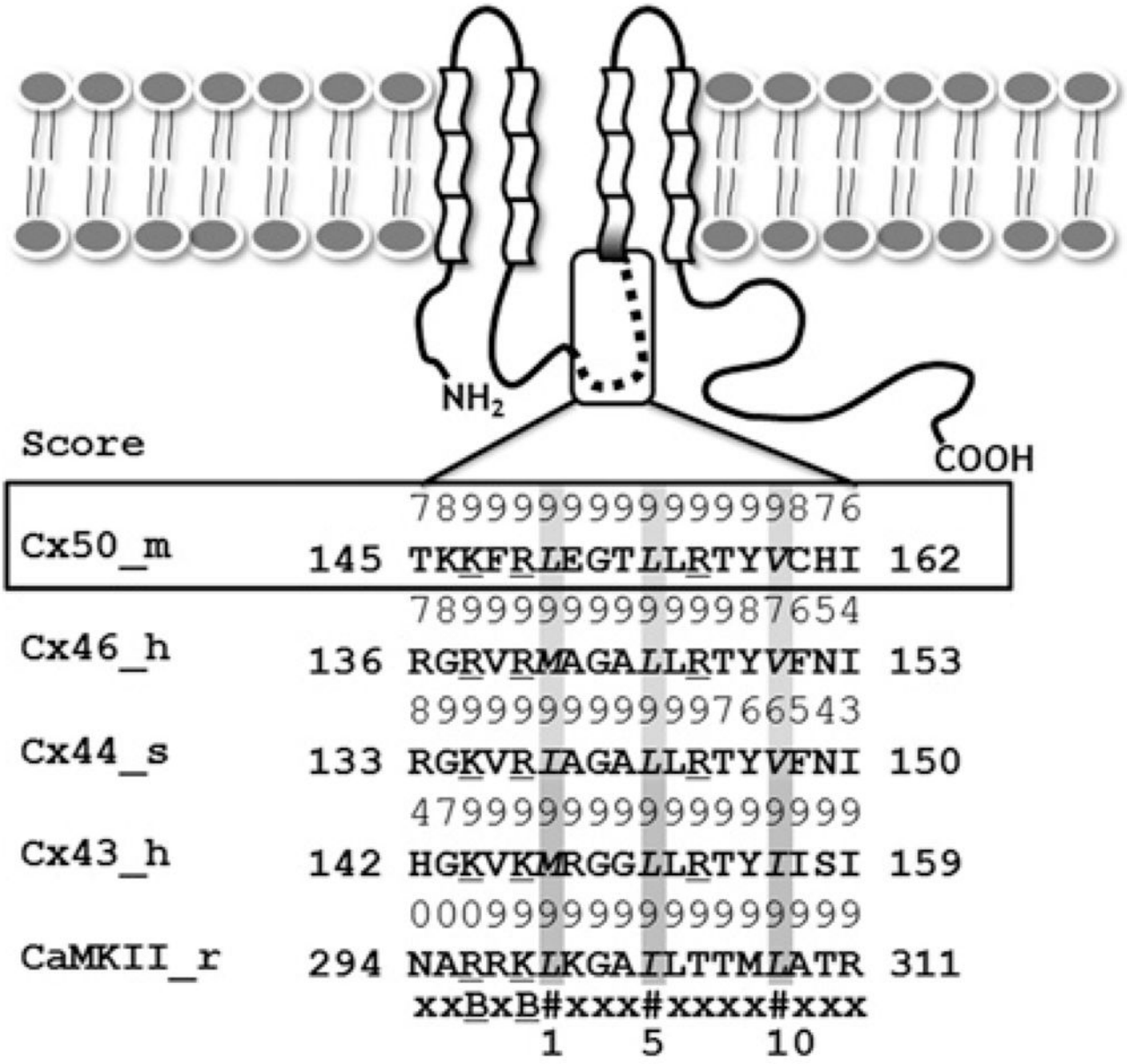


**Figure 1. Cxs membrane topology and the putative CaM-binding sites**

The $\alpha$-class of Cxs are composed of four transmembrane segments, two extracellular loops, one cytoplasmic loop, a short N-terminus and a much longer C-terminal tail. The predicted CaM-binding sites are located in the second half of the intracellular loop between TM2 and TM3. The numeric score (1–9) represents the probability of an accurate prediction of high-affinity CaM-binding sites. The CaM-binding sequences identified in the $\alpha$-class Cxs are similar to those of CaMKII. All of the aligned sequences fit the 1–5–10 CaM-binding mode subclass, where each number represents the presence of a hydrophobic residue. m, mouse; h, human; s, sheep; r, rat; #, hydrophobic residues (highlighted in grey); B, basic residues (underscored).

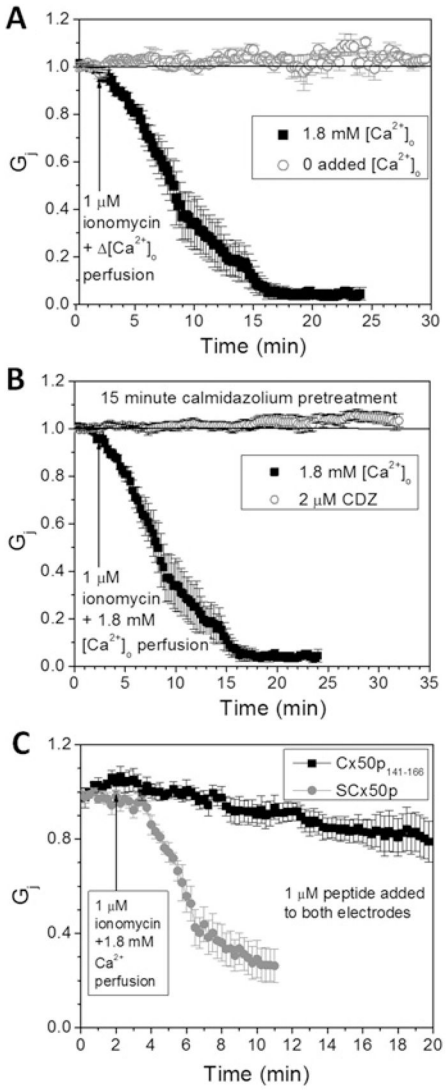


**Figure 2. $Ca^{2+}$- and CaM-dependence of Cx50 gap junction uncoupling**

(**A**) Cx50-N2a cell pair superfusion with 1 $\mu$M ionomycin bath saline with or without 1.8 mM $CaCl_2$ demonstrates a time-dependent uncoupling of Cx50 gap junctions that requires 1.8 mM $[Ca^{2+}]_o$. (**B**) Pre-treatment with 2 mM CDZ for 10–15 min before patch-clamp analysis completely prevented the 1.8 mM $[Ca^{2+}]_o$-dependent uncoupling response. (**C**) Inclusion of 1 $\mu$M $Cx50p^{141–166}$ in both whole-cell patch pipettes prevented 80 % of the $Ca^{2+}$/CaM-dependent decline in Cx50 $G_j$. In contrast, experiments performed with SCx50p prevented only 20 % of the 1.8 mM $[Ca^{2+}]_o$–CaM-dependent reduction in Cx50 $G_j$. The average ± S.E.M. initial $g_j$ values for all experimental groups are displayed in Table 1.

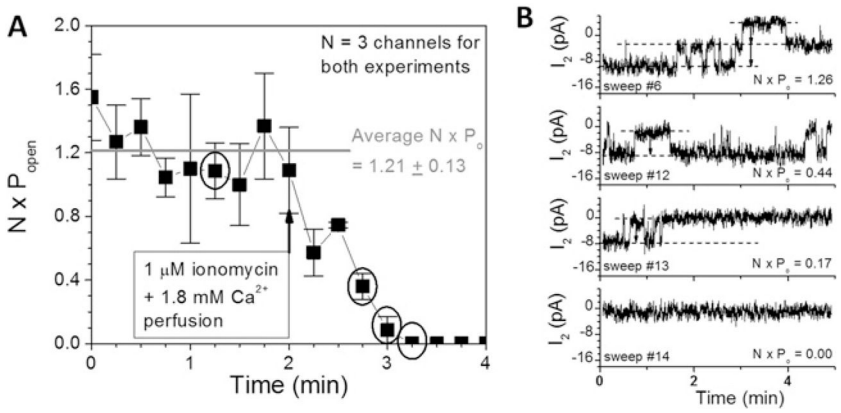


**Figure 3. Mechanistic basis for $Ca^{2+}$/CaM-dependent Cx50 gap junction uncoupling**

(**A**) The product of the number of open channels ($N$) and open probability ($P_o$) from two poorly coupled Cx50-N2a cell pairs is plotted as a function of time and 1 $\mu$M ionomycin +1.8 mM $[Ca^{2+}]_o$ superfusion. $N \cdot P_o$ declined from an average control value of 1.21 open channels to 0 within 2 min of ionomycin/$CaCl_2$ saline superfusion. (**B**) Cx50 gap junction channel current recordings from one experiment are shown for the time points indicated by the circles in (**A**). The number and duration of the open channels declined progressively to 0 without any apparent reduction in the single-channel conductance (314 pS), indicative of closure of a $Ca^{2+}$–CaM-dependent gate without a block of the ion-permeation pathway.

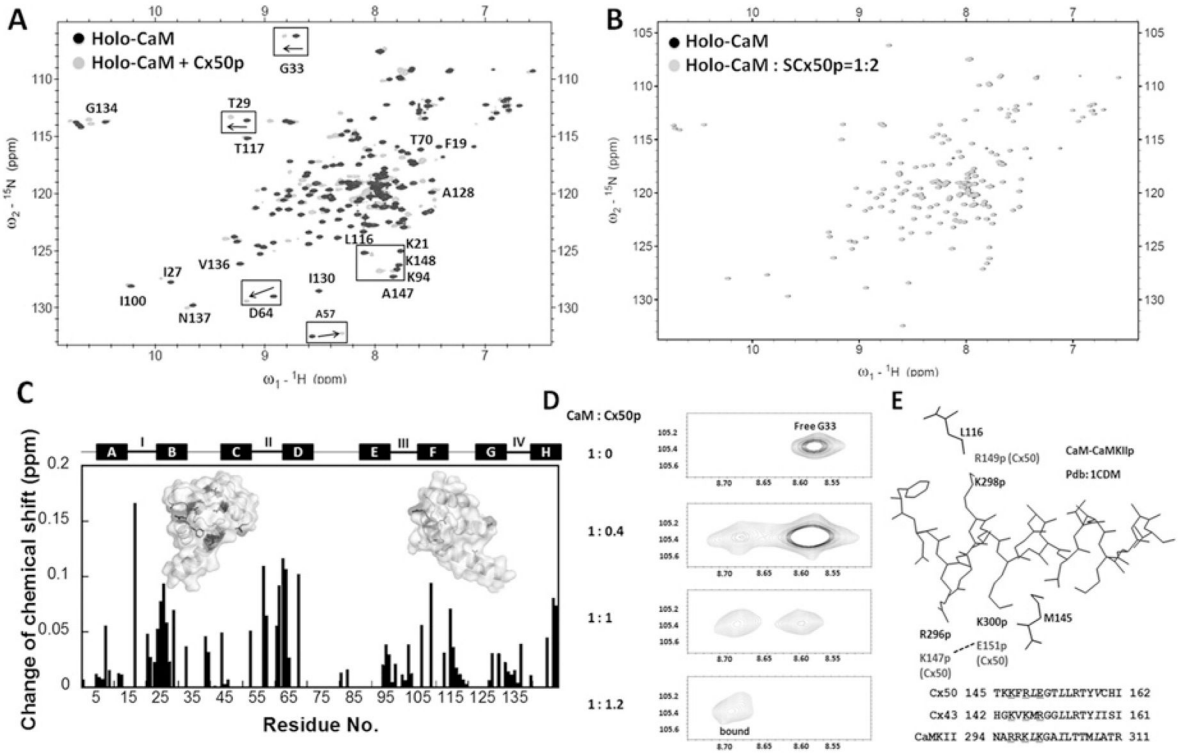


**Figure 4. Monitoring the interaction between CaM and Cx50p$^{141–166}$ by ($^{1}$H,$^{15}$N)-HSQC spectroscopy**

(**A**) An overlay of HSQC spectra of holo-CaM (black) with the spectrum of the holo-CaM–Cx50p$^{141–166}$ (grey). (**B**) An overlay of the HSQC spectra of holo-CaM (black) with the spectrum of the holo-CaM–SCx50p (grey). (**C**) Chemical-shift perturbation in CaM induced by addition of 2-fold molar excess of Cx50p$^{141–166}$. The weight-average chemical-shift change ($\Delta\delta$) was calculated using eqn (5). Residues with $\Delta\delta >$ 0.1 p.p.m. were mapped to the three-dimensional structure of holo-CaM (PDB code 3CLN). (**D**) The chemical-shift change of Gly$^{33}$ during titration of holo-CaM with Cx50p$^{141–166}$. The disappearance of the peak (free form) was accompanied by the appearance of the corresponding peak (bound form) at a new position. (**E**) Structural basis of the difference in directionality of chemical shift change. The structure of the CaM–CaMKII complex (PDB code 1CDM) is shown with the peptide (inside) and the CaM residues (outside). Leu$^{116}$ and Met$^{145}$ of CaM are within 5 Å of Lys$^{298}$p and Lys$^{300}$p of the peptide respectively. These peptide positions correspond to Lys$^{146}$p and Arg$^{148}$p for Cx43, and Arg$^{149}$p and Glu$^{151}$p for Cx50, as can be seen in the superposition of their sequences. In Cx50, Glu$^{151}$p may be pulled away from Met$^{145}$ by Lys$^{147}$p. In contrast, in Cx43, Arg$^{148}$p may be pushed towards Met$^{145}$ by Lys$^{144}$p. These differences in peptide sequences can cause changes of chemical shifts in different directions.

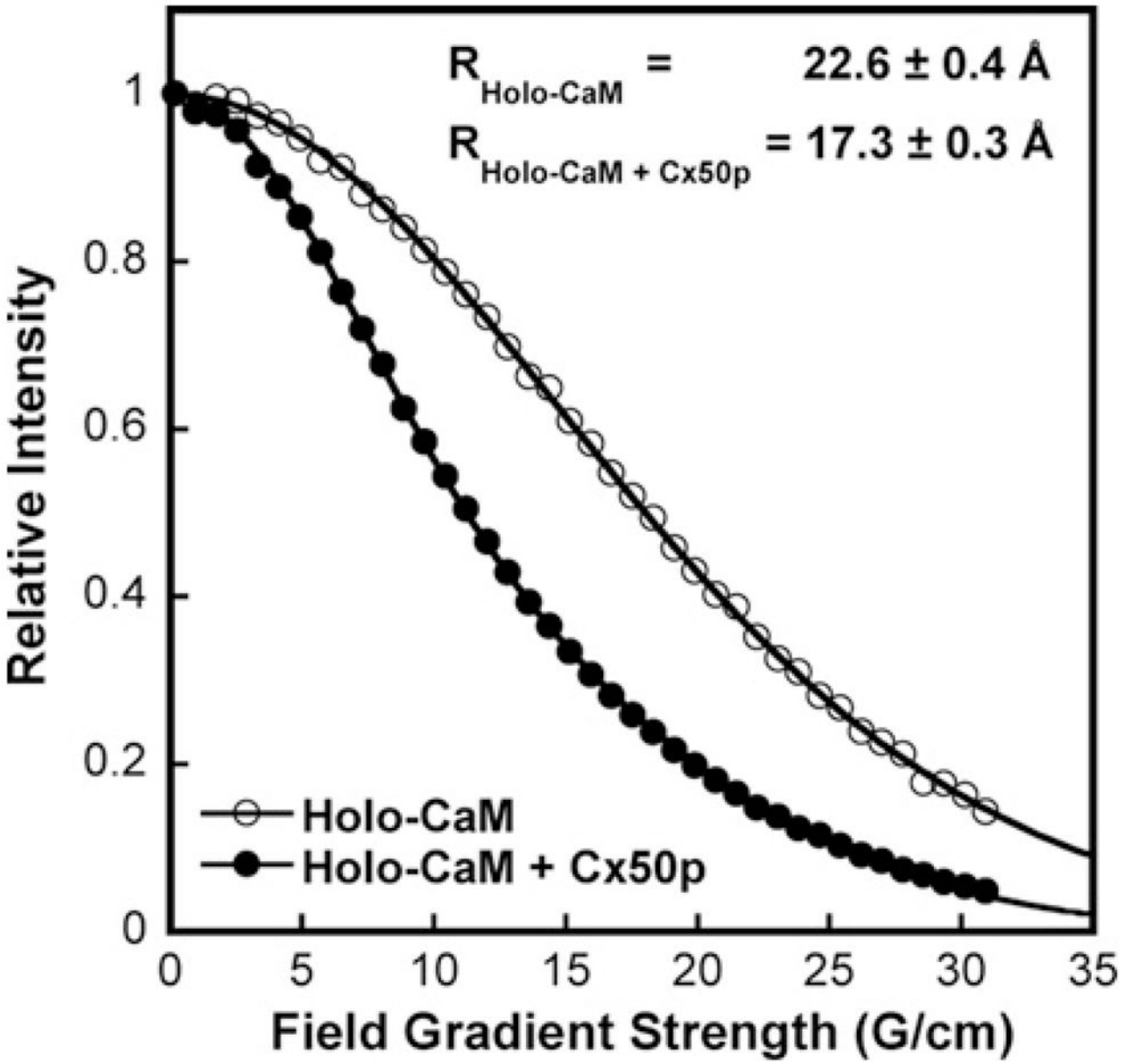


**Figure 5. Hydrodynamic radii of CaM–Cx50p$^{141–166}$ complex determination by pulse-field gradient NMR**

The NMR signal decay of holo-CaM (○) and holo-CaM–Cx50p$^{141–166}$ complex (●) as a function of field strength. The calculated hydrodynamic radii of the CaM and complexes are indicated on the top.

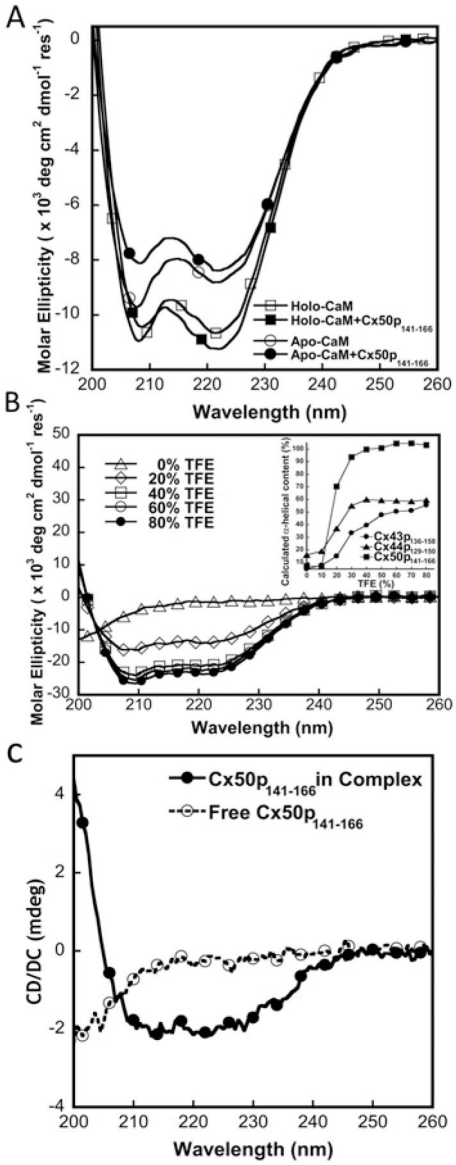


**Figure 6. CD studies of the interaction between CaM and Cx50p$^{141-166}$**

(**A**) Far-UV CD spectra of CaM in the presence of 5 mM EGTA (○, apo-CaM) or $CaCl_2$ (□, holo-CaM), and a CaM–Cx50p$^{141–166}$ (1:1) mixture with 5 mM EGTA (●, apo-CaM–Cx50p$^{141–166}$) or $CaCl_2$ (■, holo-CaM–Cx50p$^{141–166}$). (**B**) Far-UV spectra of the synthetic peptide Cx50p$^{141–166}$ with addition of TFE (0–80 %). The inset shows calculated $\alpha$-helical content as a function of TFE concentration for the peptides Cx50p$^{141–166}$ (■), Cx44p$^{129–150}$ (▲) and Cx43p$^{136–158}$ (●). (**C**) Far-UV spectra of the synthetic peptide Cx50p$^{141–166}$ with (●) or without (○) addition of CaM.

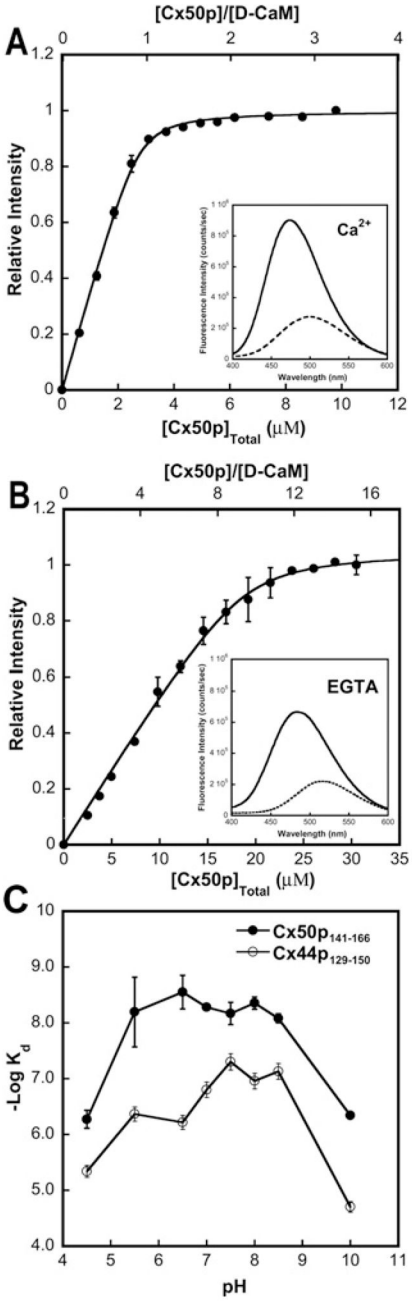


**Figure 7. Interaction of Cx50p$^{141–166}$ with D-CaM monitored by steady-state fluorescence**

(**A**) The titration curve of D-CaM (2 $\mu$M) with Cx50p$^{141–166}$ in the presence of 5 mM $Ca^{2+}$ in a buffer consisting of 50 mM Tris/HCl (pH 7.5) and 100 mM KCl. The inset shows the fluorescence spectrum of D-CaM in the absence (broken line) or the presence (continuous line) of an equivalent molar concentration of Cx50p$^{141–166}$. (**B**) Titration curve of D-CaM (2 $\mu$M) with Cx50p$^{141–166}$ in the presence of 5 mM EGTA in a buffer consisting of 50 mM Tris/HCl (pH 7.5) and 100 mM KCl. The inset shows the fluorescence spectrum of D-CaM in the absence (broken line) or the presence (continuous line) of an equivalent molar concentration of Cx50p$^{141–166}$. (**C**) pH-dependence of Cx50p$^{141–166}$ and Cx44p$^{129–150}$

binding to CaM. The binding affinities were derived from the peptide titration curves of D-CaM at various pH values. All experiments were conducted in triplicate.

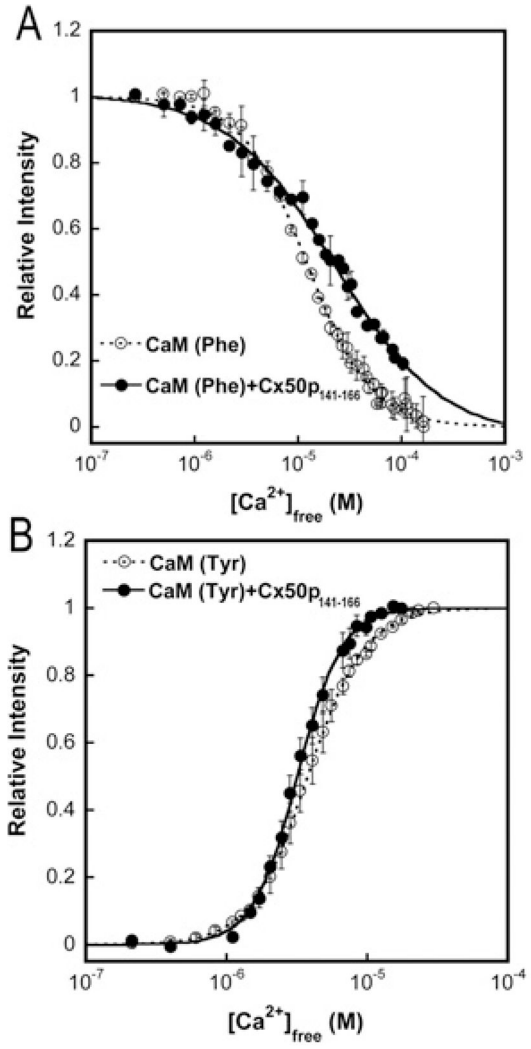


**Figure 8. Domain-specific equilibrium $Ca^{2+}$ titration of CaM (○) and CaM in complex with $Cx50p^{141–166}$ (●)**

(**A**) The intrinsic phenylalanine fluorescence ($\lambda_{ex}$ = 250 nm; $\lambda_{em}$ = 280 nm) was monitored to report the equilibrium $Ca^{2+}$-binding constants of the N-lobe of CaM. (**B**) The intrinsic tyrosine fluorescence ($\lambda_{ex}$ = 277 nm; $\lambda_{em}$ = 320 nm) was monitored to report the equilibrium $Ca^{2+}$-binding constants of the C-lobe of CaM. The free ionized $Ca^{2+}$ concentration was measured using the $Ca^{2+}$ indicator dye Oregon Green 488 BAPTA-5N. All experiments were conducted in triplicate in 50 mM Hepes (pH 7.5), 100 mM KCl, 5 mM NTA and 0.5 mM EGTA.

## Table 1

Electrophysiological measurement

| Experiment | Initial $g_j$ (nS) | *N* |
|---|---|---|
| 1.8 mM $CaCl_2$ | 9.90 ± 2.90 | 5 |
| 0 mM $CaCl_2$ | 14.74 ± 6.51 | 4 |
| 2 mM CDZ | 16.79 ± 2.95 | 4 |
| $Cx50p^{141–166}$ | 7.05 ± 2.53 | 7 |
| SCx50p | 3.36 ± 1.80 | 6 |

$g_j = I_j / V_j$ (Ohm's law, junctional current divided by transjunctional voltage). *N* = number of cell pairs recorded from each dataset.

## Table 2

Binding affinities to CaM and $\alpha$-helicity of the Cx peptides

| | $K_d$ (nM) | | $\alpha$-Helicity (%) | |
|---|---|---|---|---|
| **Peptide** | **5 mM $Ca^{2+}$** | **5 mM EGTA** | **Prediction** | **Far-UV CD measurement** |
| $Cx50p^{141–166}$ | 4.9 ± 0.6 | >8000 | 1.11 | 94 |
| $Cx44p^{129–150}$ | 49 ± 3.0 | >5000 | 1.20 | 55 |
| $Cx43p^{136–158}$ | 860 ± 20 | nd | 0.52 | 33 |

All of the experiments were conducted three times ($n = 3$). nd, not detectable. $K_d$ measurements were made of D-CaM fluorescence in 50 mM Tris/HCl (pH 7.5) and 100 mM KCl. The prediction of the helical content of peptides used the Agadir algorithm. Far-UV CD measurements were conducted using 30 % TFE in 10 mM Tris/HCl (pH 7.5) and 100 mM KCl.

## Table 3

Effects of Cx peptides binding on the metal-binding properties of CaM

| | N-domain (sites I and II) | | C-domain (sites III and IV) | |
|---|---|---|---|---|
| **Peptide** | $K_d$ ($\mu$M) | *h* | $K_d$ ($\mu$M) | *h* |
| None | 12.0 ± 0.2 | 1.4 ± 0.1 | 3.78 ± 0.03 | 2.14 ± 0.03 |
| Cx50p$^{141–166}$ | 22.7 ± 0.6 | 0.8 ± 0.1 | 3.18 ± 0.03 | 2.74 ± 0.07 |
| Cx44p$^{129–150}$ | 11.6 ± 0.1 | 1.5 ± 0.1 | 0.93 ± 0.02 | 2.20 ± 0.10 |
| Cx43p$^{136–158}$ | 14.5 ± 0.1 | 1.6 ± 0.2 | 1.16 ± 0.02 | 2.10 ± 0.10 |

All of the experiments were conducted three times ($n = 3$). $K_d$ and the Hill coefficient ($h$) were obtained by fitting the titration curve to eqn (7). Phenylalanine fluorescence ($\lambda_{ex}$ = 250 nm; $\lambda_{em}$ = 280 nm) reports the $Ca^{2+}$ binding to the N-domain of CaM. Tyrosine fluorescence ($\lambda_{ex}$ = 277 nm; $\lambda_{em}$ = 320 nm) reports the $Ca^{2+}$ binding to the C-domain of CaM.